Electronic Supplementary Material (ESI) for Energy & Environmental Science.

Supporting information

Optimal Facet Assembly of Multi-Transition Metals Layered Cathodes toward Superior Li-Ion Kinetics and Structural Stability

Feng Zou,‡[a] Jae-Bum Kim,‡[a] Jiliang Zhang,[b] Gi-Hyeok Lee,[c] Lulu Lyu,[a] Jun-Hyeok Choi,[d] Timo Kankaanpää,[e] Yong Min Lee[df] and Yong-Mook Kang*[agh]

[a.] *Department of Materials Science and Engineering, Korea University, Seoul 02841, Republic of Korea.*
[b.] *School of Materials Science and Engineering, Dalian Jiaotong University, Dalian 116028, P. R. China*
[c.] *Advanced Light Source, Lawrence Berkeley National Laboratory, Berkeley, CA, United States.*
[d.] *Department of Energy Science and Engineering, Daegu Gyeongbuk Institute of Science and Technology (DGIST), Daegu 42988, Republic of Korea*
[e.] *Umicore Battery Materials Finland Oy, 67101, Kokkola, Finland*
[f.] *Department of Chemical and Biomolecular Engineering, Yonsei University, 50 Yonsei-ro, Seodaemun-gu, Seoul 03722, Republic of Korea*
[g.] *KU-KIST Graduate School of Converging Science and Technology, Korea University, Seoul, 02841 Republic of Korea.*
[h.] *Department of Battery-Smart Factory, Korea University, Seoul 02841, Republic of Korea*

***Corresponding author,**
E-Mail address: dake1234@korea.ac.kr (Y.-M. Kang)

Experimental Methods

Materials synthesis

Synthesis of NCM111 crystal particles via co-precipitation of TM oxalate precursor. Transition metal solution A (0.03 M) was prepared by dissolving 0.01 mol of stoichiometric $NiSO_4 \cdot 6H_2O$, $CoSO_4 \cdot 7H_2O$, and $MnSO_4 \cdot H_2O$ (>99%, Sigma-Aldrich) in deionized water. To produce solution B, 0.03 mol of sodium oxalate (>99%, Samchun Chemical) was dissolved in distilled water. Solution B was added dropwise to solution A at a rate of 1 ml min^{-1} while subjected to ultrasonic dispersion at 180 W. The dropping process was carried out under a microwave heating with 60 W, and the mixed solution was maintained at 60 °C for 20 h. To remove dissolved ions, the precipitate was filtered and washed multiple times with deionized water and ethanol. The particulates were dried in a vacuum oven at 60 °C for 8 h. The resultant transition metal oxalate precursors were then mixed with three lithium salts at a concentration of 120% (>99%, Sigma-Aldrich, at least 20% excess to compensate for Li loss at high temperatures): (1) Pure LiCl, (2) Pure $LiNO_3$, and (3) 1:2 LiCl-$LiNO_3$. Annealed for 10 h at 825 °C. The black powder was rinsed multiple times with deionized water and ethanol to remove excess lithium salt following the reaction. The washed particulates were dried in a vacuum oven at 60 °C for 24 h to get three NCM111 products with distinct facets.

Material characterization

X-ray diffraction (XRD) patterns of the samples collected at room temperature using a laboratory X-ray diffractometer (Rigaku Ultima IV with Cu Kα radiation) and synchrotron XRD (Pohang Light Source II (PLS−II) 3D XRS beamline) . Convert the collected 2D diffraction images into 1D patterns using Fit 2D software. [1, 2] Hard X-ray absorption spectroscopy (hXAS) spectra of Ni, Mn, and Co K edges were collected at the 7D beamline of PLS-II. Perform standard data reduction procedures using Athena software to plot XAS spectra. [3] The final structural model was visualized by VESTA software. [4] Simulation program used was COMSOL Multiphysics (ver. 6.0), [5] which is based on Finite Element Method (FEM) for multiphysics analysis.

Inductively coupled plasma atomic emission spectrometry (ICP-AES, OPTIMA 8300, Perkin-Elmer) was used to measure the transition metal and lithium contents in the three samples. X-ray photoelectron spectroscopy (XPS) measurements of the samples were collected on a spectrometer (Shimadzu, Japan). All binding energies were corrected using the C signal at 284.5 eV as standard.

The morphological information of the samples was collected by field emission scanning electron microscope (FE-SEM) (JEOL JSM-7800F) and field emission transmission electron microscope (FE-TEM) (JEM-F200).

For cycled electrode measurements, the cells were disassembled, and the electrodes were washed with dimethyl carbonate (DMC) to clean. Atomic resolution cold FEG transmission electron microscopy (Cs-TEM) was performed by using a JEOL JEM-

ARM200F. Atomic resolution images were obtained using a High Angle Annular Dark Field (HAADF) detector. Electron energy loss spectroscopy (EELS) is performed with a Gatan quantum detector.

Electrochemical measurement

In the half-cell electrochemical performance measurement, NCM111 active material was mixed with acetylene black and polyvinylidene fluoride (PVDF) in a ratio of 8:1:1 in N-methyl pyrrolidone (NMP) solvent to prepare an electrode slurry for electrochemical testing. The resulting slurry was coated onto aluminum foil and dried in a vacuum oven at 120 °C for 5 h. The electrodes were then stamped into disks with a radius of 0.6 cm. The positive electrode, Celgard 2325 membrane separator and lithium metal sheet were assembled into a CR2032 button cell in an argon-filled glove box. A solution of 1 M $LiPF_6$ in ethylene carbonate and diethyl carbonate (EC/DEC) (1:1, v/v) was used as the electrolyte for all cells. All electrochemical tests were performed at room temperature using a WonATech system. Galvanostatic charge/discharge cycling was performed over a voltage range of 2.5−4.5 V (vs. Li/Li ions). The galvanostatic intermittent titration (GITT) technique was performed after the initial charge cycle. In the GITT procedure, the battery is operated in the range of 2.5−4.5 V, discharged and charged with a 10-minute pulse of 20 mA g^{-1}, and then rested for 1.5 h.

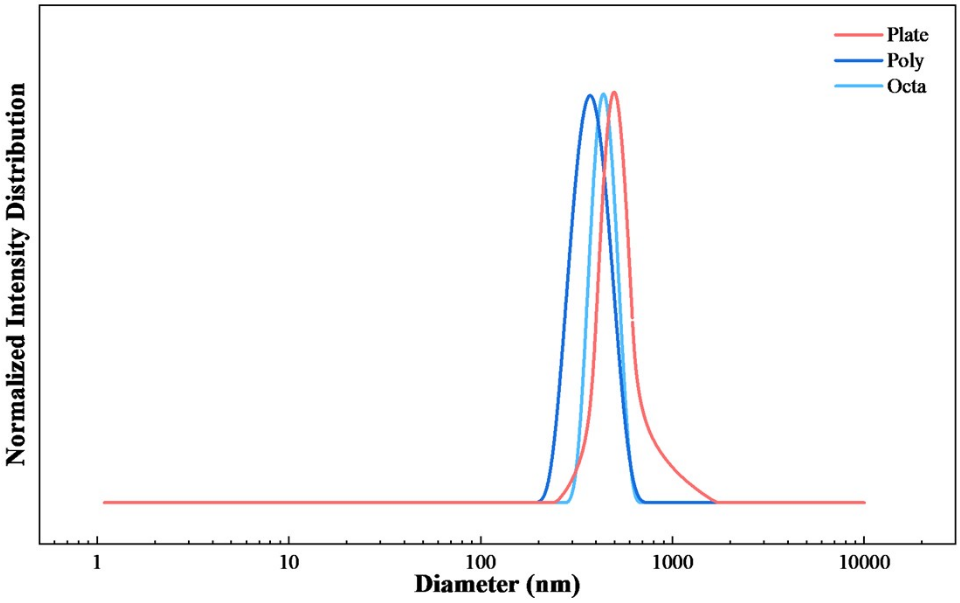

Fig. S1 Normalized particle size distribution of three NCM111 crystals

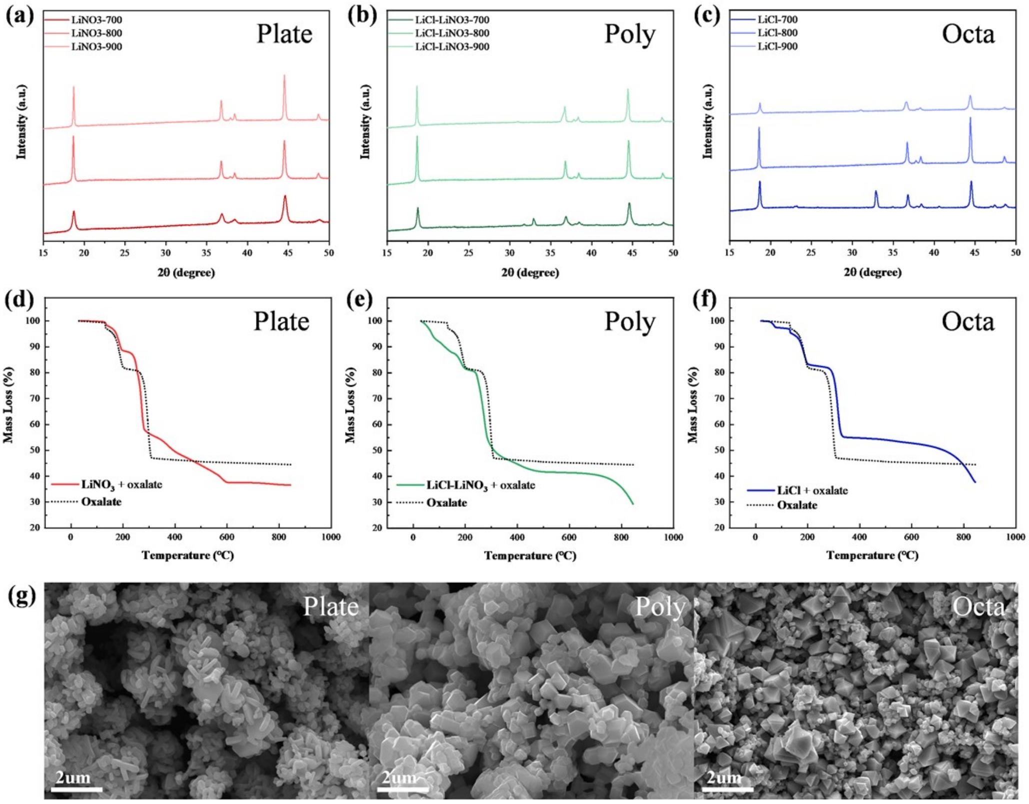

Fig. S2 XRD data (CuKα) of three morphological NCM111 single particles with different temperature: (a) Plate ($LiNO_3$), (b) Poly ($LiCl$-$LiNO_3$), (c) Octa (LiCl). TGA curve of NCM111 single particles with different morphology on the (d) Plate ($LiNO_3$), (e) Poly ($LiCl$-$LiNO_3$), (f) Octa (LiCl). (g) SEM images of three NCM111 crystals.

Analysis of the powder diffraction patterns (Fig. S2a, b, c) reveals that the samples containing LiCl formed impurity-containing *R*-3*m* structures below 700 °C and at 800 °C, no impurities were detected in any of the samples. Above 900 °C, the diffraction peaks of all three samples began to broaden and suggesting a decrease in crystallinity.
TGA measurements of the mixtures of the selected precursors and lithium sources were performed using an open crucible in an oxygen atmosphere (Fig. S2 d, e, f). The general decomposition process of these mixtures started at about 120 °C. At higher temperatures, approximately between 100 and 400 °C (depending on the content of $LiNO_3$ in the precursor), a combustion process occurred: it involved the oxidation of TM $^{2+}$ to TM $^{3+}$ and the thermal decomposition of oxalate. Depending on the LiCl content in the lithium source, when the temperature exceeded 700 °C, the mass began to lose in the final stage, which involved the decomposition reaction of LiCl, indicating that LiCl participated in the reaction as a lithium source after this stage.
During the sintering process, the formation of specific facets in NCM111 is influenced by the chemical potential of the lithium salts used. Due to thermodynamic constraints, only three (003)/ (104)/ (012) facets can stably exist. The (003) facets decrease as the lithium chemical potential increases, while an increase in the oxygen chemical potential produces more (012) facets. The (104) facets have the lowest surface energy and are insensitive to both the lithium and oxygen chemical potentials. [6] By adjusting the

composition of the mixed lithium source containing both LiCl and $LiNO_3$, the melting point of the mixture of lithium source can be adjusted by the used salts like $LiNO_3$ and LiCl, thereby regulating the lithium chemical potential in the system. It is possible to achieve polyhedral shapes that vary between these two extremes. By using three different lithium sources in Table. S1, we obtained independent particles of single crystal materials in octahedral, polyhedral, and plate-like shapes.

As shown in Fig. S2(g), depending on the lithium salt used，the three final samples showed specific morphological features in the SEM images: plate, polygon and octahedron. All the NCM111 single particles were named according to the morphological features. The samples show particle sizes of 100−1000 nm with clearly defined crystal structures.

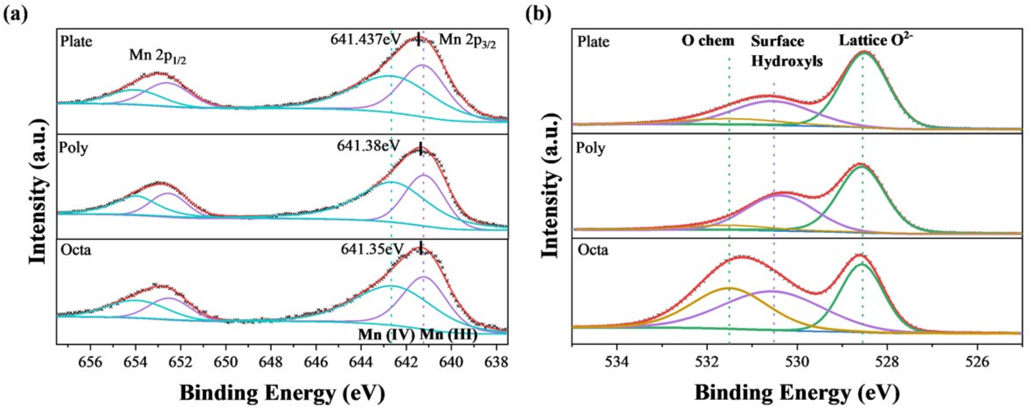

Fig. S3 XPS spectra of NCM111 samples with different exposed facets, (a) Mn 2p partial spectra and (b) O 1s spectra.

To check the valence state and distribution of elements. The transition metals were determined using X-ray photoelectron spectroscopy (XPS) analysis of the original Ar-etched samples. Representative XPS spectra of Mn are shown in Fig. S3(a). In addition, the spectral descriptions of Co and Ni based on the chemical composition of the NCM are shown in Fig. S3. The main peak broadening of the Mn 2p 3/2 photoelectron spectra at 641.4 eV and 653.0 eV indicates the presence of Mn^{3+} and Mn^{4+} on the surface of all samples, with Mn^{3+} predominating. In addition, as the (012) crystalline facets content increases in the Octa, the spectra shift toward the lower energy band, but the gap 0.087 eV is below the error value 0.1 eV and cannot indicate an obviously decrease in in the valence state of Mn.

The O 1s spectrum of NCM111 in Fig. S3(b) exhibits two peaks: the a-peak at 528.5 eV corresponding to the metal-oxygen bond O^{2-}, and the peak at 530.3 eV between lattice oxygen O^{2-} and oxygen-containing surface chemicals is more due to the TM 1s and 2p (or higher) transitions reflecting the uncoordinated TM signatures. Higher ratio of (012) facet is more polar and likely to produce the increased corresponding signal. It usually needs to be attributed to signals from hydroxyl groups (chemisorbed hydrogen) on the exposed metal oxide surface. [7] In the Octa, which has the highest content of (012) facets, an additional peak at 531.5 eV appears, typically associated with surface adsorbed by-products like water or carbon dioxide. Given that argon etching removed most surface by-products, these results suggest that the surface by-product layer on Octa is thicker than in other samples. This could be due to the increased reactivity of the (012) facet.

.

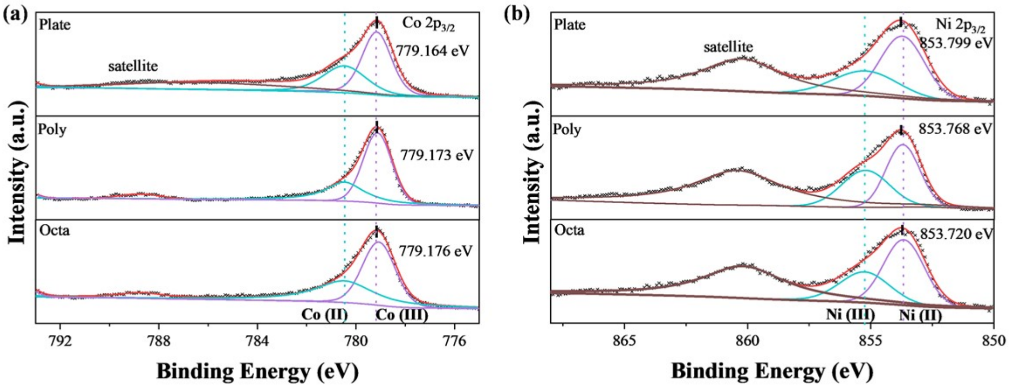

Fig. S4 XPS spectra of NCM111 samples with different exposed facets, (a) Co $2p_{3/2}$ partial spectra and (b) Ni $2p_{3/2}$ partial spectra.

As shown in Fig. S4, the peak positions of Co $2p_{3/2}$ and Ni $2p_{3/2}$ spectra exhibit a high degree of consistency across all three samples. For these three samples, the Co $2p_{3/2}$ spectrum peaks at about 779.3 eV, accompanied by the weak satellite peaks at about 788.7 eV, indicating the presence of Co^{3+}. Additionally, peaks at 781.3 eV point to the coexistence of Co^{2+}. The Ni $2p_{3/2}$ spectrum shows sharp peaks at 853.8 eV, with weak satellite peaks at 860.0 eV, indicative of Ni^{2+}. One less prominent peak at 855.3 eV suggests the presence of a small amount of Ni^{3+}.

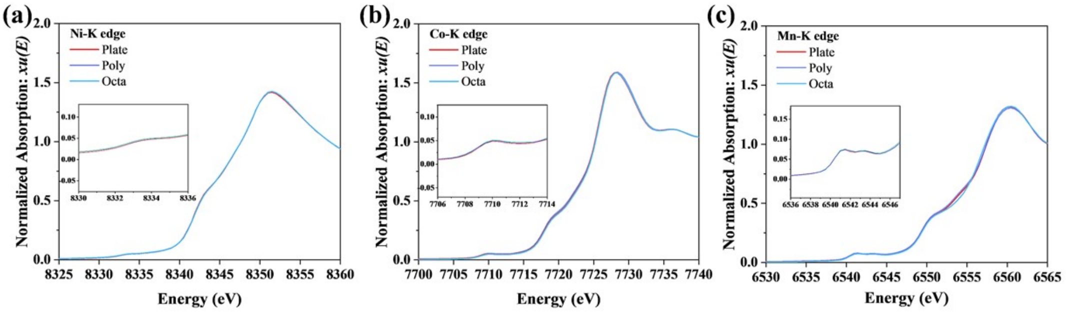

Fig. S5 XAFS spectra of NCM111 single particles with different exposed facets. (a) Ni K-edge, (b) Co K-edge, (c) Mn K-edge.

Internal chemical changes were studied using synchrotron XAS with depth analysis capability to examine changes in the average bulk oxidation state of most samples. Fig. S5 compares the K edge spectra of Ni, Co, and Mn collected on three different morphologies of the original NCM111 single particles. Edge energy positions are typically used to indicate oxidation state. Higher energy shifts correspond to an increase in the oxidation state of the transition metal, while lower energy shifts correspond to a reduction of the transition metal. No significant energy shift is observed on the transition metal K edges, suggesting negligible differences in the chemical oxidation states of the transition metals in most bulk.

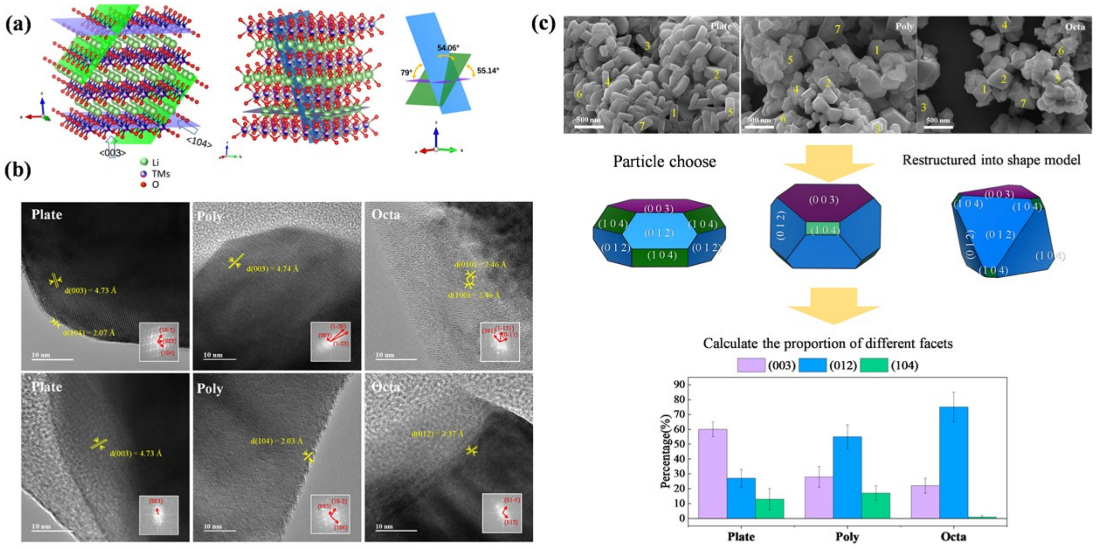

Fig. S6 (a) Geometric relationship between (003), (012), (104) three facets. (b) HRTEM images of NCM111 single particles with different morphology in (003), (012), (104) facets. (c) Three-dimensional reconstruction of NCM111 samples according to the relationship between a specific crystal morphology and the proportion of facets.

Fig. S6(a) illustrates that in the crystal structure, the (003) facet is parallel to the Li and TM plates and impermeable to lithium ions. In contrast, both the (012) and (104) facets, terminating with alternating TM-O-Li layers, are permeable to lithium. Notably, the (012) facet exhibits the highest surface energy, while the (104) facet has the lowest. The relationship between crystal morphology and the Wulff shape is also depicted in Fig. S6(a). Using the (003) crystal facet as a reference, the angles between the (003)-(012) and the (003)-(104) facets are 79 degrees and 55.14 degrees, respectively. Given that the enclosed polyhedral shape is fixed, the (104) facet forms a rectangular shape, spanning six faces. The (012) facet, an axisymmetric polygon, also covers six faces. Meanwhile, the (003) facet, a symmetric hexagon, occupies two faces of the structure. [4, 8]

Based on Fig. S6(b), the spacing of the (003) facets in the Poly (4.74 Å) was slightly larger than that in the Plate (4.70 Å). The serrated edges forming (104) facets in the Plate (2.03 Å) and Poly (2.07 Å) resulted in blurred edges. This trend aligns well with the results obtained from XRD tests. According to the FFT measurements of the Octa, (012) was directly observed(d = 2.37 Å), another spacings of the (010) and (101) facets were both d ≈ 2.46 Å, resulting in calculated cell parameters of a = b ≈ 2.84, which are only slightly lower than the results obtained from Pawley refinement (a = 2.855). This indicates good consistency between XRD and HRTEM test results, underscoring the reliability of our structural assessments.

Furthermore, for the corresponding geometric relationships, the exposed facets can be determined. To measure the proportions of facets, we rebuilt 3D models by VESTA based on the particle shapes from SEM images. Therein, the particles with clear edges and uniform size were selected. Randomly points were picked on the image and select seven particles nearby. Although dislocations and twins are inevitably formed, the approximate growth morphology can be confirmed thanks to the similar growth environment finally facilitating the identification and quantification of the three distinct facets, as demonstrated in Fig. S6(c). By sampling and calculating the facet ratios from the SEM images and conducting the simulations with couple of particles, we could determine the final facet ratio., the content of (003) facet decreases from 60% in the plate shape to 30% in the polyhedral shape, and finally to about 20% in the octa shape. Similarly, the content of (012) facet increases from about 20% in the plate shape to not less than 50% in the octa shape, and finally reaches a proportion of about 70% in the octa shape. [9]

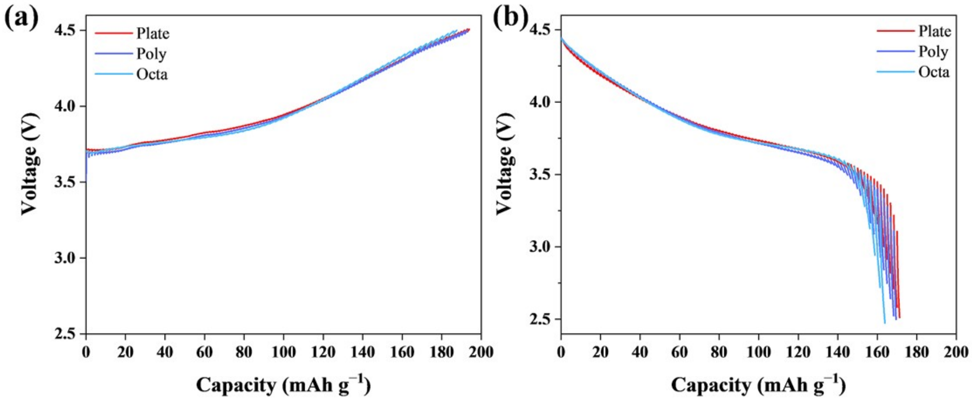

Fig. S7 GITT curves of three morphological NCM111 single particles at the second cycles. (a) charge processes, (b) discharge processes.

A specific image area was selected to identify the dislocation density. The dislocation density of the Octa sample (Fig. S9c, e) is 1~1.1×10^{-15} m^2, while that of the Poly sample (Fig. S9h, j) is 2~3×10^{-16} m^2 demonstrating that the Octa samples undergoes more serious degradation during cycling that the Poly homologues. Even if the thickness of the measured samples is not clear, the Octa sample apparently has at least 5-10 times higher dislocation density compared to the Poly homologue.

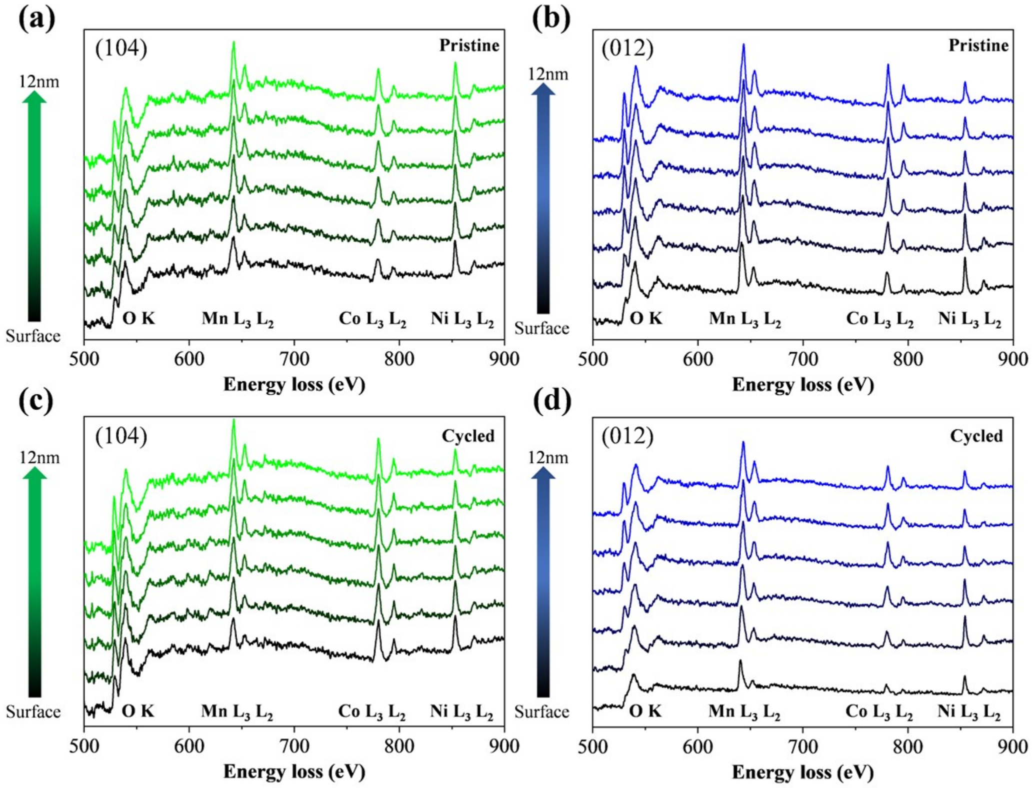

Fig. S8 EELS spectrums (1−12 nm from the surface) of the pristine and after 100 cycled Poly. The step size of EELS is 2 nm. (a) (104) facet and (b) the (012) facet in pristine sample; (c) (104) facet and (d) (012) facet in cycled sample.

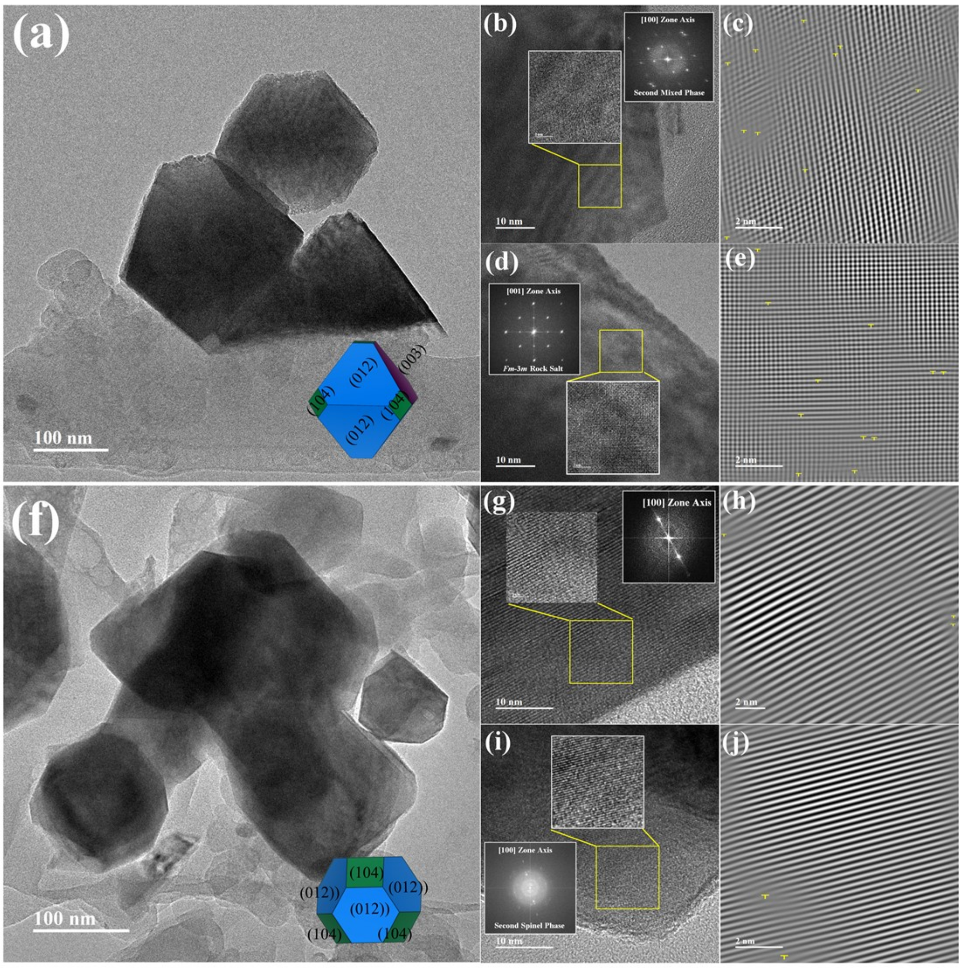

Fig. S9 HRTEM and FFT imaging demonstrating the dislocation density of NCM111 samples after 100 cycles. (a-e) The Octa, (f-j) The Poly. The perfect dislocations are marked by 'T' symbols.

After measuring different crystal particles of Octa and Poly have 100 cycles, HRTEM obtained results similar to HAADF STEM.
Wulff shape comparison confirmed the orientation of the crystal facets(Fig. S9a,f). For the Octa, further FFT analysis revealed the appearance of the second phase with a mixture spinel structure(Fig. S9b) to the typical *Fm*-3*m* structure(Fig. S9d) in the (001) direction, indicating a significantly higher degree of degradation on the (012) facet than on the Octa. In contrast, The Poly still maintain the *R*-3*m* layer structure in bulk(Fig. S8g) and some second spinel phase formed in the near edge part(Fig. S9i).

A specific image area was selected to identify the dislocation density (Fig. S9b, d, g, i). The dislocation density of the Octa sample (Fig. S9c, e) is $1{\sim}1.1\times10^{-15}$ m^2, while that of the Poly sample (Fig. S9h, j) is $2{\sim}3\times10^{-16}$ m^2 demonstrating that the Octa samples undergoes more serious degradation during cycling that the Poly homologues. Even if the thickness of the measured samples is not clear, the Octa sample apparently has at least 5-10 times higher dislocation density compared to the Poly homologue.

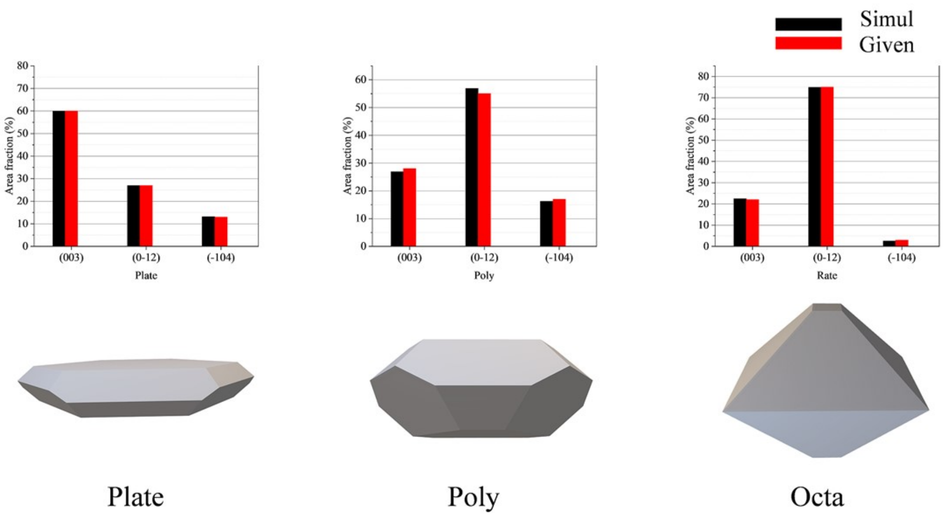

Fig. S10 Schematic diagram for the simulated structure and the structure obtained from experiments by using 3D CAD.

Simulation program used was COMSOL Multiphysics (ver. 6.0), which is based on Finite Element Method (FEM) for multiphysics analysis. To align the shape of particles for analysis with actual conditions, a 3D structure reflecting D$_{50}$ value and surface area ratio of particles was created (Fig. S10). Constant lithiation was conducted at a rate of 1C, and the material properties needed for simulation are listed in Table S3. The equilibrium potential was determined using the Galvanostatic Intermittent Titration Technique (GITT). The properties of the electrolyte are expressed as a function depending on c_l, and information from the program's material library was utilized. Within each particle, the electrochemical reactions occurring at the electrolyte/electrode interface result in the lithiation into particle. Here, the exchange current density influences the overpotential generated during reactions at each interface. Consequently, to maintain uniform overpotential during the lithiation into (012) and (104) interfaces, the reference exchange current density was kept constant in both facets and the open-circuit voltage for calculating the overpotential of each particle was consistently applied. To ensure consistency in the overpotential arising from electrical conductivity and Li$^+$ ion diffusivity within each particle, we used the same electrochemical property values. Then, simulations were carried out in two scenarios. In the first scenario, lithiation start to occur at both the (104) and (012) facets where the overpotential is measured. In the second scenario, the (012) facets were assumed to have degraded, blocking lithiation at this interface, and thereafter, the overpotential was assessed. The simulation was performed to be matched with the single NCM particle experiment that could compare the electrochemical performances of each particle. Therein, the NCM particle is in contact with an electrically connected probe, while Li metal acting as a counter electrode. The probe surface is set to contact with the (003) facet with the same area for all particles.

Lithium ion diffusion into the particle due to electrochemical reactions occurring at the electrolyte-electrode interface of a single particle was interpreted. In these electrochemical reactions of particles, potential is defined as follows:

$\eta = E_{ct} - E_{eq}$ (1)

where η represents overpotential (V), E_{ct} represents the potential of particles, and E_{eq} denotes equilibrium potential. E_{ct} satisfies the following condition:

$E_{ct} = \phi_s - \phi_l$ (2)

where Φ denotes electric potential and subscript s and l signify solid and liquid phases respectively. The electric current in the electrode follows:

$i_s = - \sigma_s \nabla \phi_s$ (3)

where i_s represents the electric current, and σ_s signifies electrical conductivity.

Ion transfer in electrolytes satisfies this equation:

$$\frac{\partial c}{\partial t} + \nabla \cdot (- D_l \nabla c_l + \frac{i_l t_+}{F}) = R_l \quad (4)$$

$$i_l = - \sigma_l \nabla \phi_l + \frac{2\sigma_l RT}{F}\left(1 + \frac{\partial \ln f}{\partial \ln c_l}\right)(1 - t_+)\nabla \ln c_l \quad (5)$$

Here σ_l denotes electrolyte conductivity (S/m), D_l signifies electrolyte salt diffusivity (m^2/s), c_l represents electrolyte concentration, i_l symbolizes electrolyte current density (A/m^2), t_+ indicates transference number, f signifies activity coefficient.

The lithium intercalation electrochemical reaction occurring at the interface between particles and electrolytes follows Butler−Volmer kinetics.

$$i_{loc} = i_0 \left(\exp\left(\frac{\alpha F \eta}{RT}\right) - \exp\left(- \frac{\alpha F \eta}{RT}\right)\right) \quad (6)$$

where i_{loc} represents interface current density (A/m^2), i_0 symbolizes exchange current density(A/m^2), α indicates transfer coefficient. i_0 changes according to material's lithiation state and concentration of electrolytes based on this equation.

$$i_0 = i_{0,ref}(T) \times \left[\left(2 \cdot \frac{c}{c_{s,max}}\right)\left(2 \cdot \frac{c_{s,max} - c}{c_{s,max}}\right)\left(\frac{c_l}{c_{l,ref}}\right)\right]^{\alpha} \quad (7)$$

Here $i_{0,ref}(T)$ is reference exchange current density depending on temperature, c is corresponding lithium concentration variable(mol/m^3), $c_{s,max}$ signifies maximum lithium concentration in active material. Electrochemical reaction happening on surface of Lithium metal also obeys Butler−Volmer kinetics where i_0 changes only by c_l at surface based on this equation.

$$i_0 = i_{0,ref}(T) \times \left(\frac{c_l}{c_{l,ref}}\right)^{\alpha} \quad (8)$$

Flux into particles due to electrochemical reactions on surface (R (mol/m^2 s)) is defined as follows:

$$R = \frac{i_{loc}}{F} \quad (9)$$

Solid diffusion inside particles adheres to Fick's law.

$$\frac{dc}{dt} + \nabla \cdot (-D\nabla c) = R \quad (10)$$

where D represents diffusivity (m^2/s).

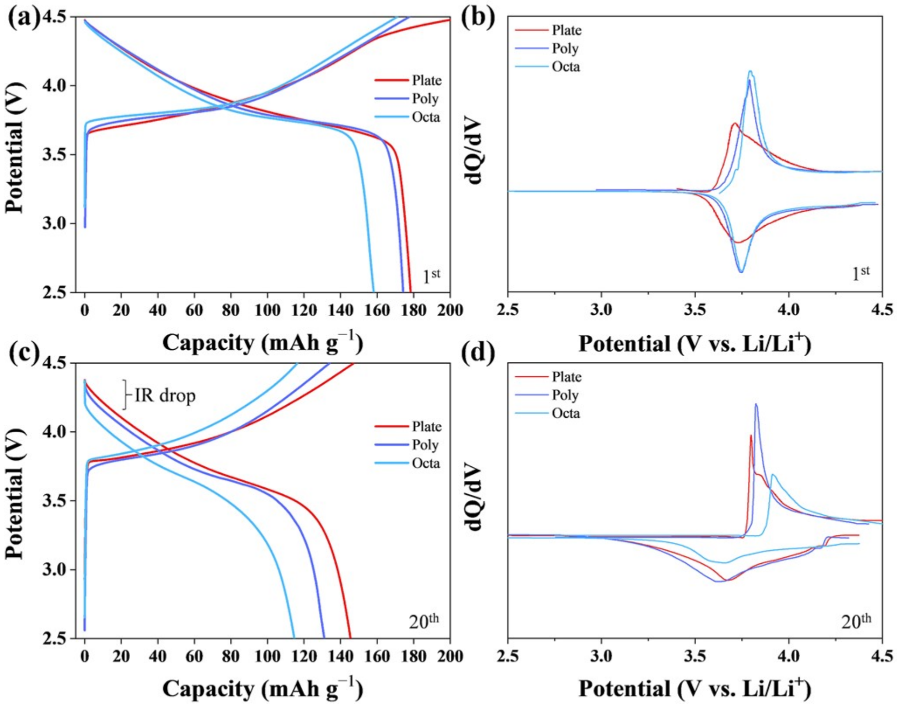

Fig. S11 Charge and discharge curve of three morphological NCM111 single particles under cut-off voltages (2.5−4.5 V) with 100 mAh g^{-1} at (a) 1st cycle and (c) after 20 cycles; the dQ/dV curves are presented respectively in (b) 1st cycle and (d) after 20 cycles.

In Fig. S11(a), demonstrates that under a mild condition of 100 mAh g^{-1}, none of the three initial samples exhibited a noticeable voltage drop, showing good reversibility in the dQ/dV plot (Fig. S11b). With increasing cycles, the charge-discharge curve (Fig. S10c) reveals a ~0.3 V decrease in the onset voltage for the Octa, suggesting more significant degradation compared to the single layer, whereas the Poly and Plate exhibit a minor voltage drop of ~0.1 V. Further analysis in the dQ/dV diagram (Fig. S11d) indicates that the Octa faces the most severe irreversible overpotential (~0.3 V), the Plate shows a minimal overpotential of ~0.1 V, and the Poly performance degrades to a level between the two.

Table S1. Elemental and particle size distributions of NCM111 single particle with different synthetic lithium source.

Samples	**Lithium source**	**ICP result (Li:Ni:Co:Mn)**	**D50 Size (nm)**
Plate	$LiNO_3$	0.99:0.34:0.33:0.32	545.4
Poly	$LiNO_3$ and LiCl	0.96:0.34:0.33:0.32	358.9
Octa	LiCl	0.95:0.34:0.33:0.32	459.5

Table. S2 The oxidation states ratio of Ni, Co and Mn in NCM111 samples with different exposed facets, obtained from XPS spectra.

Sample	Ni (II: III)	Co (II: III)	Mn (III: IV)
Plate	1.717:1	0.783:1	0.751:1
Poly	1.491:1	0.708:1	0.733:1
Octa	1.638:1	0.886:1	0.791:1

The Plate sample shows the highest ratio of Ni^{2+} as well as the 2nd highest ratios of Co^{3+} and Mn^{4+}, indicating (003) looks most beneficial to keep up the overall feature of NCM111 in terms of the oxidation states of transition metals. Meanwhile, the Octa sample is composed of the lowest amount of Co^{3+} and Mn^{4+} which have the pivotal role to stabilize the rhombohedral symmetry probably because highly reactive polar (012) facets are primarily exposed. By contrast, the Poly sample keeps up the highest ratio of Co^{3+} and Mn^{4+}, which is probably attributed to the significant proportion of non-polar (104) facets. Also, we can infer that the Poly sample undergoes the lowest cation mixing between Ni^{2+} and Li^{+} because of the lowest ratio of Ni^{2+} among NCM111 homologues. However, XPS analysis is conducted on a broad scale, and thus the data presented therein only provides an average value across the three exposed facets. Considering that the acceptable error margin for XPS measurements is about 0.1eV, [16] the peak shift less than 0.1 eV does during our analysis does not look significant enough. So, rather than XPS spectra, Electron Energy Loss Spectroscopy (EELS) spectra in Fig. 4 can provide clearer distinctions at the atomic level in terms of the accuracy. Then, it can help to demonstrate the changes that might not be evident only through XPS analysis.

Table S3. Constants for Multiphysics model of NCM111 and their values from single particle measurement.

Symbol	Value	Unit	Description
$c_{s,max}$	28058	mol m^{-3}	maximum lithium concentration
σ_s	1.6	μS cm^{-1}	electric conductivity[10]
$i_{0,ref}$	0.1	A m^{-2}	reference exchange[11] current density
D	1×10^{-16}	m^2 s^{-1}	ion diffusivity

References

1. A. Hammersley, *J. Appl. Crystallogr.*, 2016, **49**, 646-652.
2. A. P. Hammersley, S. O. Svensson, M. Hanfland, A. N. Fitch and D. Hausermann, *High Pressure Res.*, 1996, **14**, 235-248.
3. B. Ravel and M. Newville, *J. Synchrotron Radiat.*, 2005, **12**, 537-541.
4. K. Momma and F. Izumi, *J. Appl. Crystallogr.*, 2011, **44**, 1272-1276.
5. S. COMSOL Multiphysics® v. 6.0.
6. J. C. Garcia, J. Bareño, J. Yan, G. Chen, A. Hauser, J. R. Croy and H. Iddir, *J. Phys. Chem. C*, 2017, **121**, 8290-8299.
7. H. Idriss, *Surf. Sci.*, 2021, **712**, 121894.
8. M. v. Laue, *Z. Kristallogr. Cryst. Mater.*, 1943, **105**, 124-133.
9. J. I. Goldstein, D. E. Newbury, J. R. Michael, N. W. Ritchie, J. H. J. Scott and D. C. Joy, *Scanning electron microscopy and X-ray microanalysis*, springer, 2017.
10. S. Burkhardt, M. S. Friedrich, J. K. Eckhardt, A. C. Wagner, N. Bohn, J. R. Binder, L. Chen, M. T. Elm, J. Janek and P. J. Klar, *ACS Energy Lett.*, 2019, **4**, 2117-2123.
11. J. S. Kim, S. Lim, H. Munakata, S. S. Kim and K. Kanamura, *Electrochim. Acta*, 2021, **390**.